A Machine Learning Empowered Shape Memory Alloy Gripper with Displacement-Force-Stiffness Self-sensing

Yong-Chen Pei[1], Bao-Hua Wang[1], Ji-Tuo Wu[1], Chenyang Wang[2], Jing-Han Guan[1*], Huiqi Lu[2]

***Abstract*—This paper proposes a multiple self-sensing gripper (MssGripper) driven by the shape memory alloy (SMA) and empowered by machine learning algorithms. The MssGripper can identify objects without external sensors. A single SMA wire can drive the gripper for self-sensing accurately. This paper confirms the resistance of the SMA can reflect the phase transition and can be used for displacement and force prediction, as well as for object stiffness prediction. Through machine learning, a backpropagation neural network (BPNN) and long-short-term-memory (LSTM) are used to establish multiple self-sensing models for prediction. The robustness experimental results show that the self-sensing models based on LSTM have higher prediction accuracy. The average root-mean-square errors of displacement prediction and force prediction are 0.063 mm and 0.236 N, respectively, and the stiffness prediction error is less than 9.4%. Moreover, the accuracy of the classifier in stiffness identification is 97.2%. The MssGripper can accurately predict the displacement, force, and stiffness and identify objects such as springs, rubber bars and steel bars. The establishment of the models expands the novel idea of gripper sensing, which is beneficial to promoting miniaturization and compactness.**

***Index Terms*—Gripper, Machine learning, Multiple self-sensing, Shape memory alloy.**

I. INTRODUCTION

GRIPPERS can grasp objects by imitating finger movements. Recent research has shown that grippers are moving towards multiple sensing [1]. Grippers with multiple sensing can obtain more information, such as force and displacement, and manipulate objects more flexibly and reliably. Some objects are sensitive to force, such as biological tissue, chips and lenses. Multiple sensing grippers can prevent damage to objects by sensing their physical properties.

For sensing methods, sensing grippers are divided into the following:

1) Gripper sensing via external sensors. Zhang et al. [2] reported a microgripper for position/force sensing using a laser displacement sensor. Rakotondrabe and Ivan [3] proposed a thermal-piezoelectric microgripper with an optical displacement sensor to measure the displacement. Moreover, Romeo et al. [4] used a force sensor to control the gripping force of the pneumatic gripper. However, sensing was realized by sacrificing the space cost. These grippers were less flexible and adaptable.
2) Grippers with integrated sensors. These grippers embed the sensor into the body. Lu et al. [5] integrated haptic sensors into the fingers and palm of the gripper to manipulate the object. Wang et al. [6] used a super-coiled polymer actuator to drive a gripper with a copper wire. The force was calculated by measuring the resistance of the copper wire. Blanes et al. [7] attached an accelerometer to the fingers of the gripper and detected position, velocity, and stiffness. Although these grippers were miniaturized, they were difficult to manufacture.
3) The self-sensing gripper allows sensing without extra external sensors; it can be programmed and miniaturized for specific tasks and applications. Ji et al. [8] developed a composite film-based gripper that could bend as well as strain sensing. Bombara et al. [9] used a twisted string actuator to achieve position self-sensing of the gripper.

Therefore, a self-sensing gripper is a good choice for simplicity and miniaturization. Self-sensing can be achieved by using smart materials with actuation and sensing capabilities in the gripper. Studies have shown that self-sensing can be achieved by SMA. As a kind of smart material, shape memory alloy (SMA) is deformed by temperature stimulation, resulting in the shape memory effect (SME). SME is caused by the transformation of the microstructure, which is composed of high-temperature austenite and low-temperature martensite. Temperature stimulation to induce SME can be achieved by various approaches, such as water-bath heating, laser heating, and Joule heating [10], [11]. Heating low resistivity wires requires a high current source, which is expensive and an inefficient payload for the actuator [12]. However, NiTi SMAs have a high resistivity [13] and allow the electric current to activate directly. Therefore, Joule heating activation of NiTi SMA wires is convenient and simple. Lu et al. [14] developed a parallel gripper driven by an SMA actuator with a wire diameter of 0.4 mm, a clamping target diameter range of 60 to 100 mm, and a clamping force of 4 to 7.5 N. Mehrabi et al. [15] designed a micro-gripper with a size of 12 mm × 10 mm, and the maximum deflection of the jaws was 200 μm. Lee et al. [16] developed a non-embedded three-finger soft gripper with a

Yong-Chen Pei, Bao-Hua Wang, Ji-Tuo Wu and Jing-Han Guan are with the School of Mechanical and Aerospace Engineering, Jilin University, Changchun, Jilin, 130022, China. (Corresponding author: Jing-Han Guan (guanjh18@mails.jlu.edu.cn)).

Chenyang Wang and Huiqi Lu are with Institute of Biomedical Engineering, Department of Engineering Science, University of Oxford, Oxford, OX3 7DQ, United Kingdom.

bending angle of 400°, a maximum clamping force of 30 N, an SMA wire length of 300 mm and a diameter of 203 μm. In these studies, the displacement and force were obtained through external sensors. However, the self-sensing of SMA was not applied.

To exploit the driving and sensing potential of the SMA, the researchers studied the resistance characteristic. It is found that the resistivities of different crystal phases are different. During the thermal cycle, the resistance exhibits a wave-like change, and the peaks and valleys correspond to the critical points of the phase transition [17]. The method of determining the progress of the phase transition based on the resistance has realized self-sensing. The stress–strain–resistance model was built to identify the phase transition by an appropriate algorithm, and it can be used to estimate the strain and stress of the SMA [18]–[23]. Krishna Chaitanya and Dhanalakshmi [24] studied the position control of the resistive feedback SMA wire gripper, with an average error of 2.053%. Lan et al. [25] developed SMA wire-actuated finger-type micro-grippers with a clamping force of 0.49 N. Simone et al. [26] proposed an SMA gripper that can grip objects of different sizes and shapes and found that resistance can be used to predict position and force. Although many studies have investigated SMA resistance behavior, existing grippers have only focused on displacement or force sensing. The process of clamping objects requires not only jaw displacement control but also force control.

Moreover, existing research has shown that hysteresis models (Preisach model [27], Prandtl-Ishlinskii model [28], Bouc-Wen model [29]) were used to describe the hysteresis of SMA. However, the robustness of the hysteresis model is poor. Once the data become noisy and missing, the model accuracy will be drastically reduced. Compared to hysteresis models, physics-based Muller-Achenbach-Seelecke (MAS) models [30], [31] have good robustness. However, the strong nonlinearity of the MAS models may bring difficulties to the design of control systems, and these model-based control design approaches are prone to model errors due to parametric uncertainty and unmodelled dynamics [32], [33]. Therefore, researchers have used a more robust, fault-tolerant and design-friendly backpropagation neural network (BPNN) to capture the nonlinear relationship between the input and output [34], [35]. However, BPNN cannot directly identify systems with multivalued mapping models such as hysteresis. Due to the similarity of the hysteresis to the long-short-term-memory (LSTM), the LSTM was chosen for self-sensing modelling. The LSTM has memory storage ability, greater generalization, and higher robustness [36]. Therefore, it is a good choice to enable the multiple self-sensing of SMA grippers using LSTM models.

In this paper, a multiple self-sensing gripper (MssGripper) was proposed and fabricated by 3D printing, where the force and displacement can be quantitatively sensed and controlled by a single NiTi SMA wire. Furthermore, the MssGripper enabled the self-sensing of stiffness. By using machine learning methods, MssGripper can distinguish objects with different materials in almost real time (<0.003 s) during its operation. Second, the MssGipper is robust under different experimental conditions. The fabricated MssGripper has been tested with various loads, signal periods and types under different environmental temperatures. Finally, the LSTM model empowers the multiple self-sensing of MssGripper. The results show that the LSTM model can represent the nonlinear relationship between resistance, strain and stress, and can achieve higher accuracy than the traditional hysteresis model, polynomial model and BPNN model. Compared to existing self-sensing grippers, the MssGripper has more sensing capabilities, better robustness and contains fewer numbers of SMA wires. Moreover, the MssGripper does not require any external sensors, making the MssGripper system lighter in weight and smaller in size.

The research contents of this paper are as follows: Section II describes the structure and working principle of the MssGripper. Section III builds self-sensing models for predicting displacement, clamping force and stiffness and classifying objects. Section IV includes the experimental results. The work is summarized in Section V.

II. Design Of The SMA Wire Gripper

The MssGripper was proposed to achieve multiple self-sensing capabilities based on resistance. The design of the MssGripper included the preparation of the drive units and the manufacture of the gripper.

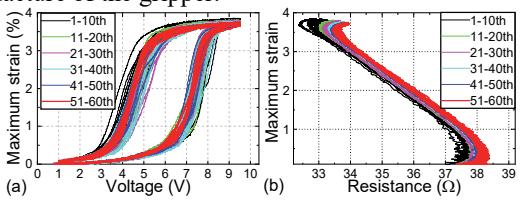

Fig. 1. Hysteresis and strain of the SMA wire during pretraining. (a) Hysteretic loops between voltage and strain. (b) Hysteretic loops between resistance and strain.

A. Preparation of the SMA wire

The thermomechanical characteristics of SMA wires approached a steady state after thermal cycles [37]. Therefore, the pretraining of SMA wires is necessary. The setup used to characterize the SMA was a gantry frame structure with suspended SMA wire. The upper section of the SMA wire was fixed, and the lower end was connected to a mass. The setup measured the displacement of the mass by a laser displacement sensor and had a resistance test system. The NiTi SMA wire with a two-way shape memory effect (manufactured by Wuhang Stainless Steel Materials Co., Ltd) has a diameter of 0.1 mm and a length of 310 mm. The prestress was 238 MPa, which limited the generation of the R-phase [38]. When the SMA was activated by Joule heating, the SMA contracted and drove the mass moving upwardly. After cooling, the mass moved downwards as the SMA elongated. The excitation signal was a symmetrical triangular wave with a peak voltage of 9.5 V and a frequency of 0.05 Hz. In addition, previous studies showed that SMA wire can be activated within 0.2 s and has a strain increase of 1.5% at the excitation signal of 1 Hz. Fig. 1 demonstrates the resistance and strain of the SMA wire during thermal cycling pretraining. The resistance determined whether

the SMA wire was fully activated to prevent overheating [17]. After 60 cycles, the maximum strain was 3.5%, and the resistance in the 100% austenite phase was 33.86 Ω. In Fig. 1(a), the strain hysteresis loop shows a convergence trend, which means that the characteristics of the SMA wire are stable. In Fig. 1(b), the strain and resistance were in a stable state.

B. Manufacturing of the MssGripper

The MssGripper was fabricated based on the pre-trained SMA wire, as shown in Fig. 2. Based on resistance characteristics, the MssGripper was used to study multiple self-sensing. All components were fixed on the vertical linear guide by sliders. Only slider 3 could slide up and down. The restrainers fixed sliders 1, 2, and 4 on the guide. An SMA wire started from slider 1 and returned to slider 1 around the groove bearing of slider 3. The upper jaw was fixed on slider 2, and the lower jaw was fixed on slider 3. When the SMA wire shrank, the lower jaw was driven upwards and approached the upper jaw. The range of the jaw was from 0 mm to 11 mm.

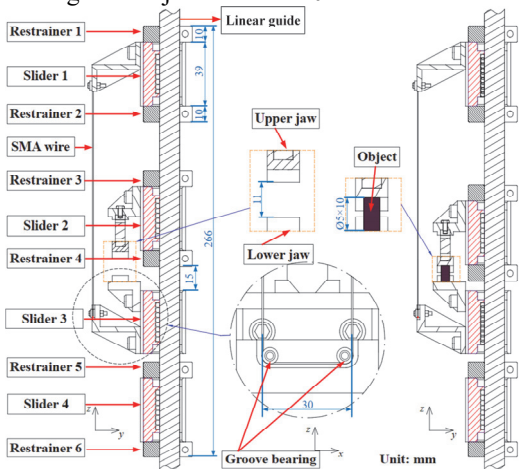

Fig. 2. Design of the MssGripper.

The actual picture of the MssGripper is shown in Fig. 3(a), including a linear guide, jaws, SMA wire, and measurement and signal acquisition system. The force sensor was connected and fixed with the upper jaw to test the clamping force F. The laser displacement sensor was placed under the lower jaw, and the displacement of the lower jaw was measured. For light weight, the guide and slider were fabricated of aluminum alloy, the jaws and support were PLA (polylactic acid), and the connecting bolts were stainless steel. In Fig. 3(b), the working steps of the MssGripper include the following:

i. The MssGripper was activated by Joule heating, and then the SMA wire contracted. Thus, the gap between the jaws was gradually reduced. Meanwhile, the reading of the laser displacement sensor ΔL increased. During the process, the jaws were not closed, and the force sensor indicated zero, $F = 0$ N;

ii. The jaws were closed, and ΔL reached the maximum. Meanwhile, the SMA wire continued to be energized, and the distance between the jaws did not change. Thus, the clamping force F gradually increased;

iii. When the clamping force F reached the maximum, the SMA was completely phase-transformed. ΔL and F were all the maximum. Then, the heating power was gradually reduced, and the wire was cooled;

iv. The MssGripper returned to the initial state (i). Meanwhile, the distance between the jaws reached the maximum, and ΔL and F were all zero.

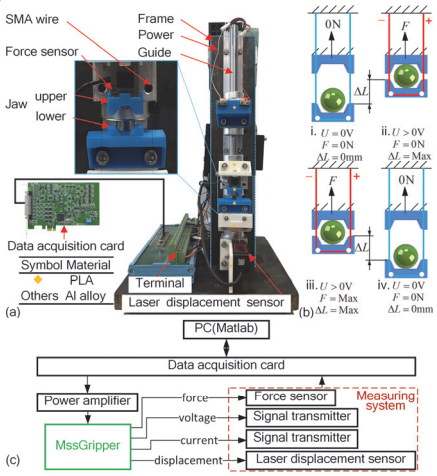

Fig. 3. The MssGripper. (a) Actual picture. (b) Working principle. (c) Experimental setup.

TABLE I
PARAMETERS OF THE SMA WIRE.

Symbols	Parameters	Values
A_s	Austenite start temperature	75.4 °C
A_f	Austenite finish temperature	90.7 °C
M_s	Martensite start temperature	49.6 °C
M_f	Martensite finish temperature	19.9 °C
L_{SMA}	Length	310 mm
D_{SMA}	Diameter	0.1 mm

C. *Experimental setup of the MssGripper*

Fig. 3(c) shows the experimental setup of the MssGripper. A program was written in MATLAB to generate the voltage signal that was applied to the SMA wire via a data acquisition card (ADVANTECH PCIE-1816/H) and power amplifier. Then the measurement system collected and transmitted the sensing signals to the PC via a data acquisition card. The function of the signal transmitter (accuracy: 0.2% FS) is to isolate and convert the activating voltage and current of SMA wires and then output the voltage and current sampling signal. Thus, the voltage and current signals can be obtained without affecting the wire activating circuit. The displacement was measured by a laser displacement sensor (ZLDS100 L, measuring range: 10 mm, resolution: 0.01% FS), and the force signal was measured by a force sensor (measuring range: ±10 N, sensitivity: 1.0 to 2.0 mV/V). The SMA wire parameters are listed in Table I. The parameters A_s, A_f, M_s, and M_f were determined by differential scanning calorimeter (DSC, Q2000, TA Instrument, U.S. A) [39]. We used and cleaned 20 to 50 mg of SMA wires. Wires were placed in DSC, and protected by 10 to 50 ml/min nitrogen. Wires were heated to 150 °C, where they were held for three minutes for thermal equilibrium. Then, the DSC measurement started by cooling to 0 °C at 5 °C/min. At 0 °C, the wires were again held for 3 min and then heated to 150 °C with a heating rate of 5 °C/min. The latent heat of the phase transition causes the heat flow to crest or trough. The

tangent line was placed on the curve through the inflection point. A_s, A_f, M_s, and M_f were obtained from the intersection of the tangent line and the baseline of the curve.

III. Modeling of Displacement-Force-Stiffness Multiple Self-Sensing

The self-sensing of the MssGripper was achieved by using resistance and excitation signals as input. The MssGripper can realize displacement-force prediction and stiffness identification without external sensors. However, there is a nonlinear relationship between resistance and strain during the phase transition in Fig. 1. Therefore, neural networks with adaptive and non-linear advantages can be exploited to model the multiple self-sensing of the MssGripper. In addition, the strain is influenced by both the current input and the previous state. The strain curve of the SMA exhibits a hysteresis with memory storage in Fig. 1. The LSTM allows the prediction of displacement-force curves because of memory capability. The LSTM used current and past data as input to predict the current output. Therefore, the model based on LSTM can reduce the prediction error caused by nonlinearity and hysteresis.

D. Data preparation

The original signals were noisy, so the data were subjected to moving average filtering [9]. Moving-average filtering is a low-pass filter that can be used for real-time detection. The mean of the continuously sampled data with a window length of N_{span} was calculated. Then, this means is used as the filtered value of the median. The mathematical expression for the filtering is [38]

$$y_y(n)=\frac{y\left(n-\frac{N_{span}-1}{2}\right)+y\left(n-\frac{N_{span}-1}{2}+1\right)+\cdots+y\left(n+\frac{N_{span}-1}{2}\right)}{N_{span}} \quad (1)$$

where y is the original sampled data, yy is the filtered sampled data, and n is the position of the sampled data. The order of the filter is N_{span} = 13. The sampling frequency f is 128 Hz. The delay is (N_{span}-1) / (2f) = 0.047 s. Then, the resistance was divided into two stages by resistance phase transition detection, RPTD [38]: the transition stage was the region between the beginning of austenite transformation and the end of martensitic transformation; the remaining regions were marked as non-transition stages. Since no strain occurs in the non-transition regions, the measurement data of the transition stage were selected as the dataset. Fig. 4 shows the data preparation. In step I, the voltage and current of excitation signals were collected. Ohm's Law was used to calculate resistance. Signal calibration details can be found in [17]. In step II, RPTD detected the phase transition points P_{As} and P_{Mf} in the resistance sequence. P_{As} and P_{Mf} are the starts and endpoints of transformation, respectively. In step III, the resistance sequence was segmented through P_{As} and P_{Mf}. Orange yellow strips represent the transition stage, and the non-transition stages are represented by white strips. Then, the resistance of the transition stage is substituted into the models for prediction in step IV. Finally, the prediction data are obtained through the multiple self-sensing models in step V. Fig. 4(c) shows that the dataset is divided into a validation set, a training set and a test set at a ratio of 1:4:5. The calibration dataset consisted of an 80% training set and a 20% validation set. The training set was used to train the model, and the function of the validation set was tuning the hyperparameters of the model by internal evaluation performance. The test set was used to evaluate the accuracy and generalization ability of the model.

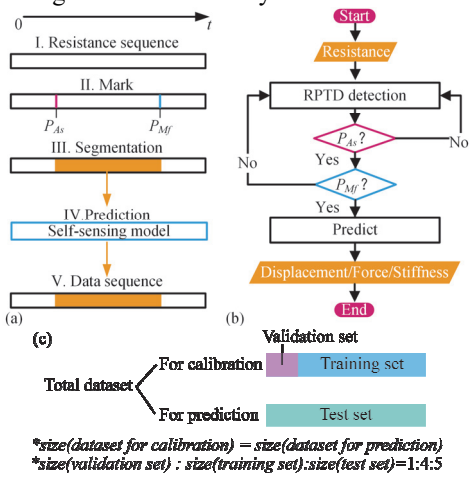

Fig. 4. Multiple self-sensing processes. (a) Procedure steps. (b) Flow chart. (c) Total dataset of self-sensing.

E. Hyperparameter optimization

Bayesian optimization is an adaptive hyperparameter search method that predicts the next combination that may bring the greatest benefit [40]. Moreover, Bayesian optimization has been widely used for hyperparameter tuning of machine learning algorithms [41]–[43]. The multiple self-sensing of the MssGripper belongs to regression and classification problems. Therefore, Bayesian optimization was deployed to optimize the hyperparameters of the self-sensing models. The hyperparameters included the number of hidden layers, the number of neurons in the hidden layers, batch size, number of epochs, dropout rate, learning rate, and activation functions. The data used for optimization were the training and validation sets. The optimization was performed based on a 5-fold cross-validation, which resulted in better generalization performance of the model. The objective function was the root-mean-square error (RMSE) on the validation set, which was evaluated 50 times. Finally, the optimized best model was tested using the test set to evaluate generalization error.

F. Displacement self-sensing model (DSM)

The displacement sensing of the MssGripper was obtained by the displacement self-sensing model (DSM). The displacement and resistance were obtained from the variable displacement and constant load experiments. DSM used the voltage and resistance as inputs and the displacement as output to build the model. The BPNN and LSTM were used for sensing modelling. The BPNN consisted of an input layer, two hidden layers and an output layer in Fig. 5(a). The input layer variables are resistance and voltage. The number of nodes in the hidden layer is l. The output of the hidden layer is [34]

$$H_j^t = f\left(w_{ij}x_t + a_j\right) \quad i = 1,2,\cdots,l, j = 1,2,\cdots,l \tag{2}$$

where f is the activation function of the hidden layer, w is the weight between the input and hidden layers, and a is the threshold of the hidden layer. The predicted output of the output layer is [34]

$$O_k^t = \sum_{j=1}^{l} H_j^t p_{jk} - b_k \quad k = 1,2,\cdots,q \tag{3}$$

where p is the weight between the hidden and output layers, and b is the threshold of the output layer. The cost function is [34]

$$E_t = \frac{1}{2}\sum_{k=1}^{l}\left(O_k^t - Y_k^t\right)^2 \tag{4}$$

where Y_k^t is the actual output. The weights and thresholds are updated as E_t, and the learning rate η is adjusted to update the iteration step size. The iteration stops when the cumulative error of the training set reaches the stopping condition. The BPNN architecture was designed using the function *newff* in MATLAB.

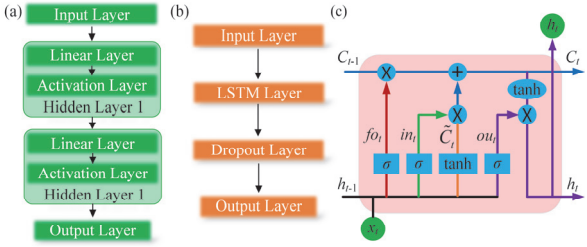

Fig. 5. The architectures of neural networks. (a) BPNN. (b) LSTM. (c) LSTM layer.

LSTM solves the problem of gradient disappearance and gradient explosion during training. Time-series data can save the information related to the context, which is similar to the hysteresis of the SMA wire [44]. Fig. 5(b) shows the architecture diagram of the LSTM, which was designed using the Deep Learning Toolbox in MATLAB 2021a. The LSTM consists of an input layer, an LSTM layer, a dropout layer and an output layer, as shown in Fig. 5(b). The dropout layer was used to prevent overfitting during training [45]. The LSTM layer introduced the concept of cells and gates, which consists of the cell state C, input gate in, forgetting gate fo, and the output gate ou [44] in Fig. 5(c). The input gate is [44]

$$in_t = \sigma\left(W_{xi}x_t + W_{hi}h_{t-1} + b_i\right) \tag{5}$$

where W_{xi} is the weight between the input x_t and in_t, W_{hi} is the weight between the hidden value h_{t-1} and in_t, b_i is the threshold of in_t, and σ is the sigmoid function. The candidate cell used for updating is [44]

$$\tilde{C}_t = \tanh\left(W_{xc}x_t + W_{hc}h_{t-1} + b_c\right) \tag{6}$$

where W_{xc} is the weight between x_t and $\tilde{C}_t$, W_{hc} is the weight between h_{t-1} and $\tilde{C}_t$, and b_c is the threshold of $\tilde{C}_t$. The forgetting gate is [44]

$$fo_t = \sigma\left(W_{xf}x_t + W_{hf}h_{t-1} + b_f\right) \tag{7}$$

where W_{xf} is the weight between x_t and fo_t, W_{hf} is the weight between h_{t-1} and fo_t, and b_f is the threshold of fo_t. The current cell state can be calculated from C_{t-1}, in_t, fo_t, and $\tilde{C}_t$, [44]

$$C_t = fo_t * C_{t-1} + in_t * \tilde{C}_t \tag{8}$$

The output gate is [44]

$$ou_t = \sigma\left(W_{xo}x_t + W_{ho}h_{t-1} + b_o\right) \tag{9}$$

where W_{xo} is the weight between x_t and ou_t, W_{ho} is the weight between h_{t-1} and ou_t, and b_o is the threshold for ou_t. The final output value is the same as the hidden value, as follows [44]

$$y_t = h_t = ou_t * \tanh\left(C_t\right) \tag{10}$$

where y_t is the output value and h_t is the hidden value. Moreover, Table II gives the parameters of the BPNN and LSTM in the DSM. The input data matrix size is 2×2049 (2049 data points).

TABLE II
PARAMETERS OF THE BPNN AND LSTM IN THE DISPLACEMENT SELF-SENSING MODEL.

BPNN		LSTM	
Items	Values	Items	Values
Number of hidden layers	2	Number of hidden layers	1
Number of hidden layer neurons	(15, 15)	Number of hidden layer neurons	99
Epochs	150	Epochs	150
Learning rate	0.0098	Learning rate	0.024018
Hidden layer transfer functions	('tansig', 'tansig')	Solver	Adam
Output layer transfer function	'purelin'	Drop probability	0.4
Training function	'trainrp'	Batch size	20

G. Force self-sensing model (FSM)

The force self-sensing of the MssGripper was obtained by the force self-sensing model (FSM). The clamping force and the resistance were obtained from the constant displacement condition. According to the one-dimensional constitutive equation of the SMA, the mechanical properties during phase transition presented as changes in stress and strain. Therefore, the FSM can also use the BPNN and the LSTM which were used to predict the clamping force. The parameters of BPNN and LSTM in FSM are the same as those of DSM in Table II.

H. Stiffness self-sensing model (SSM)

Different from displacement and force self-sensing, stiffness perception refers to predicting the stiffness coefficient of objects. Under the stiffness identification, the resistance was affected by the deformation and the force, which produced a complex change trend. Fig. 6 shows five objects to be identified with different stiffnesses. The objects included rubber bodies, stainless steel bars, and springs with three different stiffness coefficients. In the SSM, the resistance was collected and used as input to complete the classification. DSM and FSM are regression problems, while the stiffness self-sensing model (SSM) is a regression and multi-classification problem. Stiffness self-sensing requires both object classification and stiffness prediction. First, the objects in Fig. 6 were detected by a stiffness classifier. The BPNN classifier completes the classification of the objects in Fig. 7. The BPNN classifier consists of two hidden layers. The dimension of the input data is 141, and the size of the dataset is 141×200. Table III gives the parameters of the BPNN under stiffness classification.

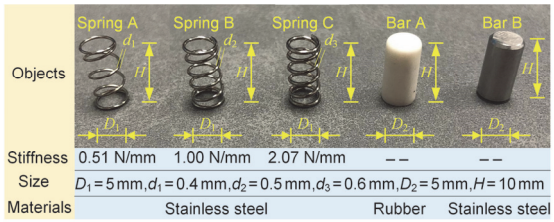

Fig. 6. Five objects to be classified and their parameters.

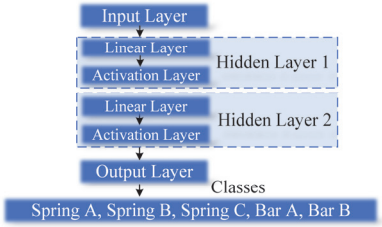

Fig. 7. Flow chart of the classifier.

TABLE III
PARAMETERS OF THE BPNN UNDER STIFFNESS CLASSIFICATION.

Items	Values	Items	Values
Number of hidden layers	2	Gradient threshold	1
Number of hidden layer neurons	(40, 40)	Hidden layer transfer functions	('logsig', 'logsig')
Epochs	50	Output layer transfer function	'purelin'
Learning rate	0.001	Training function	'trainrp'

Second, in the stiffness prediction, the DSM and FSM were used to predict displacement $\Delta\mathbf{x}$ and force $\Delta\mathbf{F}$, respectively. The displacement and force curves were segmented at equal time intervals to calculate the stiffness. According to the stiffness of each segment, it was judged whether it was a constant stiffness (spring, steel bar) or variable stiffness (rubber) object. $\Delta\mathbf{x}$ and $\Delta\mathbf{F}$ can be expressed as

$$\Delta\mathbf{x} = f_d\left(\mathbf{R},\ \mathbf{U}\right),\ \Delta\mathbf{F} = g_f\left(\mathbf{R},\ \mathbf{U}\right) \tag{11}$$

where f_d is the functional form of the DSM, g_f is the functional form of the FSM, $\mathbf{R}$ is the resistance sequence, and $\mathbf{U}$ is the voltage sequence.

Taking the number of interval points as t, $\Delta\mathbf{x}_i$, and $\Delta\mathbf{F}_i$ corresponding to each segment are expressed as

$$\Delta\mathbf{x}_i = \left[x_{it+1},\cdots,x_{(i+1)t}\right],\ \Delta\mathbf{F}_i = \left[F_{it+1},\cdots,F_{(i+1)t}\right],\ i=0,1,\cdots \tag{12}$$

According to (12), the stiffness corresponding to each segment is expressed as

$$k_i = \frac{1}{t-1}\sum_{m=2}^{t}\frac{\Delta\mathbf{F}_i(m)}{\Delta\mathbf{x}_i(m)} \tag{13}$$

Therefore, the stiffness k of the object is $k=\frac{1}{n}\sum_{i=0}^{n-1}k_i$, where n is the number of segments.

IV. EXPERIMENTS AND DISCUSSIONS

A. Experiments of the Multiple Self-Sensing Model

The prediction accuracy of the proposed multiple self-sensing models for displacement-force-stiffness was verified by robustness experiments. The variables in the robustness experiments are the environmental temperatures, loads, signal periods and types in Table IV. The environmental temperatures were 28 °C and 18 °C, above and below M_f, respectively. The driving signals of each group are shown in Fig 8. In groups A, B and D, the MssGripper was excited by a stepped voltage, as shown in Fig. 8(a). The voltage was increased by 1.9 V every 2 s, and the peak was 9.5 V. In Fig. 8(b), the voltage step was 3.2 V. In Fig. 8(c), the randomly generated voltage period was 22s. For each experimental condition, the predictions of the BPNN and LSTM for the MssGripper are compared separately at the constant load condition, constant displacement condition, and variable displacement and load condition. In addition, each group of experiments was repeated 100 times to verify the repeatability of the MssGripper self-sensing.

TABLE IV
PARAMETERS FOR ROBUSTNESS EXPERIMENTS.

Group	Environmental temperature / °C	Period / s	Load / g	Type
A	28	22	120	Step
B	18	22	120	Step
C	28	14	120	Step
D	28	22	370	Step
E	28	22	120	Random

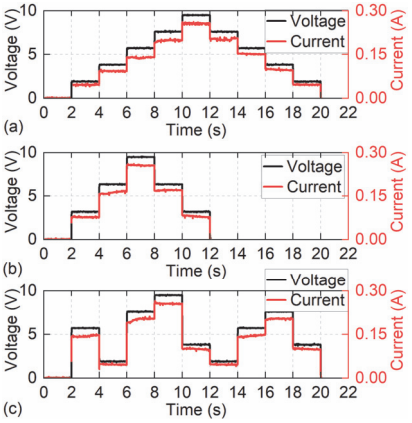

Fig. 8. The driving signals of each group. (a) Groups A, B and D. (b) Group C. (c) Group E.

B. Displacement Prediction

To verify the prediction accuracy of the DSM, the displacement of the jaw was obtained by constant load experiments. The maximum relative displacement of the jaws was 3.0 mm. In Fig. 9, the measurements of relative jaw displacement were compared to predictions. Fig. 9 shows the displacement prediction results of groups A-E, respectively. The prediction results based on the BPNN and LSTM were in good agreement with the experiments. Since the resistance was related to the phase transition, the LSTM-based prediction curves fit the actual displacement curves better than the BPNN-based prediction curves. The time series feature of LSTM effectively eliminated data outliers in displacement curves. For groups A-E, the mean RMSE of the LSTM was 0.066 mm, 0.052 mm, 0.059 mm, 0.102 mm and 0.091 mm, respectively. The mean RMSE of the BPNN was 0.242 mm, 0.276 mm, 0.178 mm, 0.301 mm and 0.166 mm, respectively.

The total mean RMSE of the LSTM-based DSM was 0.074 mm, whereas the total mean RMSE of the BPNN-based DSM was 0.233 mm. For displacement prediction, the accuracy of the LSTM was 215% = (0.233/0.074-1)×100% higher than that of the BPNN. The prediction results of LSTM under different experimental conditions all showed good accuracy and were more stable than those of BPNN. Therefore, LSTM is more suitable for DSM.

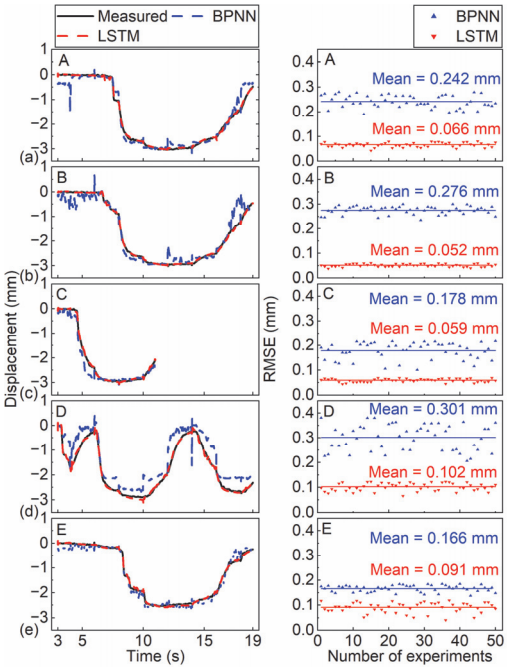

Fig. 9. Displacement prediction results of the DSM. (a). Group A. (b) Group B. (c). Group C. (d) Group D. (e) Group E.

C.Force Prediction

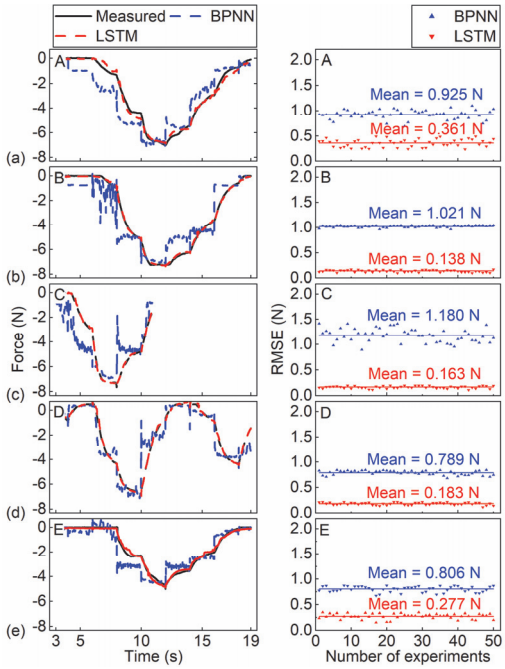

Fig. 10. Force prediction results of the FSM. (a). Group A. (b) Group B. (c). Group C. (d) Group D. (e) Group E.

To verify the prediction accuracy of the FSM, the clamping force was obtained by constant displacement experiments. The maximum clamping force of the jaws was 7.65 N. Fig. 10 shows the comparison results between the measured value of the clamping force and the predicted value of the FSM. For the BPNN, the predicted force curve is stepped, which indicates that the BPNN is affected by the step voltage. The force output is interfered by the inherent characteristics of the input neurons. The LSTM shows good agreement with the measured curves. For groups A-E, the mean RMSE of the LSTM was 0.361 N, 0.138 N, 0.163 N, 0.183 N and 0.277 N, respectively, while the mean RMSE of the BPNN was 0.925 N, 1.021 N, 1.180 N, 0.789 N and 0.806 N, respectively. The total mean RMSE of the LSTM-based FSM was 0.224 N. The total mean RMSE of the BPNN-based FSM was 0.944 N. The accuracy of the LSTM was 321% = (0.944/0.224-1)×100% higher than that of the BPNN. Therefore, LSTM is more suitable for FSM. Moreover, the accuracy improvement of LSTM for predicting force is more significant than the displacement prediction.

D.Displacement-Force Prediction

The DSM and FSM of the MssGripper were proven to be effective. However, the constant load experiments and constant displacement experiments were special cases. During the actual works of the MssGripper, the jaws were used in variable displacement and load states. The displacement and force predictions were obtained by the DSM and FSM, respectively. Fig. 11 shows the displacement measured and predicted results.

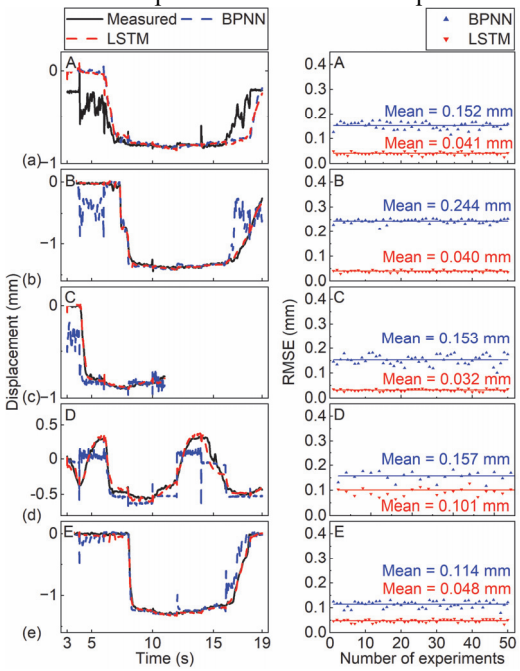

Fig. 11. Displacement prediction results of the variable displacement and load experiments. (a). Group A. (b) Group B. (c). Group C. (d) Group D. (e) Group E.

The mean displacement prediction accuracies of the BPNN- and LSTM-based DSMs were 0.164 mm and 0.052 mm, respectively. For group A, the displacement prediction accuracies of the DSM based on the BPNN and LSTM were

0.152 mm and 0.041 mm, respectively. For groups B-E, the mean RMSE of LSTM was 0.040 mm, 0.032 mm, 0.101 mm, 0.048 mm, respectively, while the mean RMSE of LSTM was 0.152 mm, 0.244 mm, 0.153 mm, 0.157 mm, and 0.114 mm, respectively. The mean force prediction accuracies of the BPNN- and LSTM-based FSMs were 0.945 N and 0.248 N, respectively, as shown in Fig. 12. The accuracy of the LSTM-based FSM was 3.8 times that of the BPNN-based FSM. The mean RMSE of the LSTM-based FSM in groups A-E was 0.323 N, 0.119 N, 0.167 N, 0.400 N and 0.233 N, respectively. The mean RMSE of the BPNN-based FSM in groups A-E was 0.937 N, 0.805 N, 1.480 N, 0.902 N and 0.600 N, respectively. Moreover, the displacement prediction accuracy was five times higher than the force prediction accuracy.

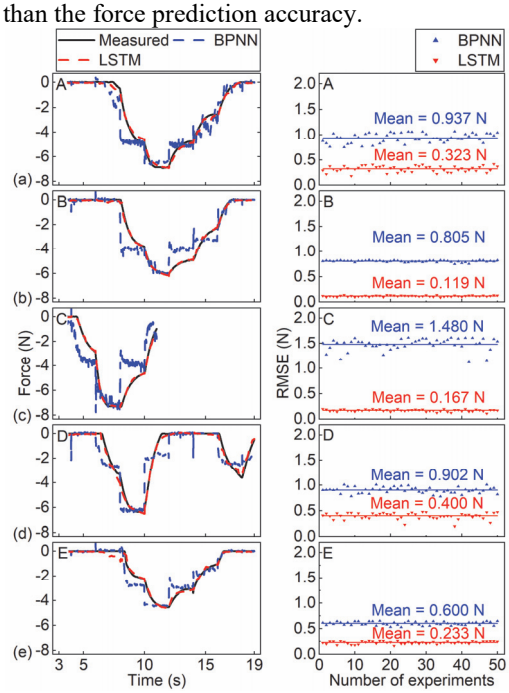

Fig. 12. Force prediction results of the variable displacement and load experiments. (a). Group A. (b) Group B. (c). Group C. (d) Group D. (e) Group E.

E. Stiffness classification and prediction

In the stiffness classification and prediction, the objects were first classified. Then, the object stiffness was predicted. When classifying objects, the total amount of data in the training set was 500. Each object class had 100 groups of data. The features were one-dimensional, and only the resistance was used as input. The data of the test set included 250 groups. In Fig. 13(a), the confusion matrix was used to evaluate the accuracy of the classifier by the BPNN. Row labels represent the true class of objects, and the sum of the data in each row is the number of each true class. Column labels represent the predicted class, and the sum of the data in each column is the number of each predicted class. The main diagonal elements were the number of correct classifications, and the remaining elements were the number of misclassifications. The average classification accuracy was 97.2%. When clamping objects with different stiffnesses, the resistance of SMAs changed significantly, resulting in high classification accuracy. Only one set of data was misclassified as Spring B. The stiffness of the spring is relatively close, so it is easy to be misidentify.

Since the stiffness of Bar B was large and could be distinguished easily from the other objects, only the stiffnesses of Spring A, Spring B, Spring C, and Bar A were predicted. Fig. 13(b) shows the comparison between the measured and predicted object stiffnesses. The stiffness of springs are almost constant. For Bar A of rubber, the stiffness increased due to material nonlinearity. Therefore, the stiffness prediction of each object was divided into two parts. The experimental results show that the SSM distinguished the variable object stiffness. The prediction errors of the Spring A, Spring B, Spring C, and Bar A models were 9.4%, 2.3%, 6.0%, and 5.6%, respectively. The stiffness predicted is close to the measured stiffness. Therefore, stiffness self-sensing realized the classification and prediction of stiffness by the SSM.

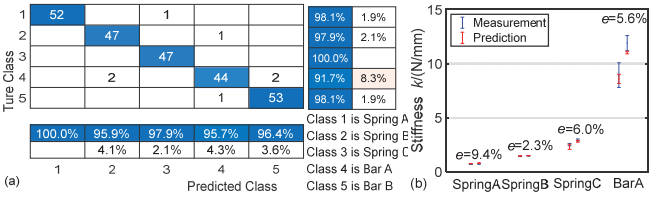

Fig. 13. Stiffness classification and prediction results for the SSM. (a) Confusion matrix of classification. (b) Comparison of prediction stiffness.

F. Discussion

The prediction accuracy of the LSTM is much better than that of the BPNN. LSTM solves the problem of abnormal input signals, while BPNN does not. For the SSM, five kinds of objects with different stiffnesses are effectively distinguished by the BPNN. Moreover, the object stiffness classes are predicted. Robustness and repeated experimental results show that model accuracy is less affected by the hysteresis and creep of SMA. The displacement and force prediction accuracy of the LSTM-based MssGripper are 0.063 mm and 0.236 N, respectively. The experimental results indicate that it is feasible to use SMA wire to drive grippers and to identify and classify objects. Multiple self-sensing based on resistance is suitable for the moving and clamping operations of the MssGripper. The MssGripper does not need the auxiliary detection of traditional sensors, such as strain gauges, but uses the resistance of the SMA wire for sensing.

The total computation time for a single experiment (2049 data points) using a computer with CPU model core i7 11800H was 0.027 s, with a peak memory footprint of 207 KB. In addition, the LSTM model had a computation time of 0.003 s for a single data point, which was suitable for real-time applications. MssGripper is compared with other works in Table V. First, the MssGripper uses fewer actuating components (SMA wires) to perform more sensing functions, including displacement, force, stiffness and classification. Second, different from the grippers [25], [26], it is verified experimentally that the MssGripper has stiffness self-sensing capability. Finally, robustness tests are carried out under different experimental conditions, including clamping states (constant displacement, constant load, and variable

displacement and load), environment temperatures, loads, signal periods and types. The test results show that the MssGripper empowered by LSTM exhibits higher accuracy and robustness than the previous SMA grippers.

TABLE V
PERFORMANCE COMPARISON OF THE PROPOSED MSSGRIPPER WITH OTHER WORKS.

References	Number of SMA wires	Self-Sensing capabilities			Robustness tests	Sensing model
		Displacement	Force	Stiffness		
[14]	8	×	×	×	★★*	×
[15]	2	×	×	×	×	×
[16]	3	×	×	×	×	×
[24]	1	√	×	×	×	Polynomial
[25]	2	√	√	Theoretical	×	Polynomial
[26]	3	√	√	Theoretical	×	Linear
This work	**1**	**√**	**√**	**√**	**★★★★★**	**LSTM**

*★ represents the number of robustness experimental conditions. A higher number means better robustness.

V. CONCLUSIONS

In this paper, an SMA wire gripper system is established, which has the capability of multiple self-sensing. Multiple self-sensing is obtained by studying the relationship between the resistance-voltage and thermomechanical characteristics of the SMA. After filtering and RPTD on the signals, the self-sensing models are established using machine learning algorithms. Machine learning methods, including the BPNN and LSTM, are used to train, predict and classify the displacement, force, and stiffness. In DSM and FSM, a good method is to use voltage and resistance as inputs and LSTM for prediction. In SSM, BPNN can achieve high accuracy in classification by using the resistance as the input. Moreover, robustness experiments show that the self-sensing of LSTM-based MssGripper is robust.

To analyze the self-sensing accuracy, additional displacement and force sensors and their attachments were involved in the current MssGripper testing system. In addition, to meet various testing requirements, the guide and frame were designed in a large size in the testing system. However, the MssGripper component used for self-sensing and driving was only an SMA wire, which can be designed in a very small size without those testing accessories. Therefore, future work will focus on miniaturization of the gripper.

REFERENCES

[1] J. Shintake, V. Cacucciolo, D. Floreano, and H. Shea, "Soft Robotic Grippers," *Advanced Materials*, vol. 30, no. 29, p. 1707035, Jul. 2018, doi: 10.1002/adma.201707035.

[2] J. Zhang, Y. Yang, J. Lou, Y. Wei, and L. Fu, "Development and Hybrid Position/Force Control of a Dual-Drive Macro-Fiber-Composite Microgripper," *Sensors*, vol. 18, no. 4, p. 1301, Apr. 2018, doi: 10.3390/s18041301.

[3] M. Rakotondrabe and I. A. Ivan, "Development and Force/Position Control of a New Hybrid Thermo-Piezoelectric MicroGripper Dedicated to Micromanipulation Tasks," *IEEE Trans. Automat. Sci. Eng.*, vol. 8, no. 4, pp. 824–834, Oct. 2011, doi: 10.1109/TASE.2011.2157683.

[4] R. A. Romeo, L. Fiorio, G. L'Erario, M. Maggiali, G. Metta, and D. Pucci, "Dynamic Control of a Rigid Pneumatic Gripper," *IEEE Robot. Autom. Lett.*, vol. 5, no. 2, pp. 2793–2800, Apr. 2020, doi: 10.1109/LRA.2020.2974446.

[5] Z. Lu, H. Guo, W. Zhang, and H. Yu, "GTac-Gripper: A Reconfigurable Under-Actuated Four-Fingered Robotic Gripper With Tactile Sensing," *IEEE Robot. Autom. Lett.*, vol. 7, no. 3, pp. 7232–7239, Jul. 2022, doi: 10.1109/LRA.2022.3181370.

[6] S. Wang, H. Huang, H. Huang, B. Li, and K. Huang, "A Lightweight Soft Gripper Driven by Self-Sensing Super-Coiled Polymer Actuator," *IEEE Robot. Autom. Lett.*, vol. 6, no. 2, pp. 2775–2782, Apr. 2021, doi: 10.1109/LRA.2021.3062578.

[7] C. Blanes, M. Mellado, and P. Beltrán, "Tactile sensing with accelerometers in prehensile grippers for robots," *Mechatronics*, vol. 33, pp. 1–12, Feb. 2016, doi: 10.1016/j.mechatronics.2015.11.007.

[8] Q. Ji *et al.*, "Dual-Responsive Soft Actuators with Integrated Sensing Function Based on 1T-MoS $_2$ Composite," *Advanced Intelligent Systems*, vol. 3, no. 7, p. 2000240, Jul. 2021, doi: 10.1002/aisy.202000240.

[9] D. Bombara, S. Fowzer, and J. Zhang, "Compliant, Large-Strain, and Self-Sensing Twisted String Actuators," *Soft Robotics*, vol. 9, no. 1, pp. 72–88, Feb. 2022, doi: 10.1089/soro.2020.0086.

[10] T. Nath, K. Akash, P. Chouhan, B. K. Lad, and I. A. Palani, "Investigation on thermo-mechanical behavior of SMA spring under the influence of different actuation medium," *Microsyst Technol*, vol. 24, no. 6, pp. 2813–2821, Jun. 2018, doi: 10.1007/s00542-017-3695-z.

[11] J.-T. Wu, Y.-C. Pei, J.-H. Guan, and C.-L. Yan, "Free Response and Musical Pitch of Shape Memory Alloy Wires Under Voltage Loading," *IEEE Trans. Ind. Electron.*, vol. 69, no. 5, pp. 5009–5017, May 2022, doi: 10.1109/TIE.2021.3076712.

[12] A. Bhattacharyya, W. L. Ables, G. K. Kannarpady, and M. A. Qidwai, "Experimental characterization of an airfoil-based actuator using high-temperature shape memory alloys," San Diego, CA, Jul. 2004, p. 118. doi: 10.1117/12.539584.

[13] W. L. Benard, H. Kahn, A. H. Heuer, and M. A. Huff, "Thin-film shape-memory alloy actuated micropumps," *J. Microelectromech. Syst.*, vol. 7, no. 2, pp. 245–251, Jun. 1998, doi: 10.1109/84.679390.

[14] Y. Lu, Z. Xie, J. Wang, H. Yue, M. Wu, and Y. Liu, "A novel design of a parallel gripper actuated by a large-stroke shape memory alloy actuator," *International Journal of Mechanical Sciences*, vol. 159, pp. 74–80, Aug. 2019, doi: 10.1016/j.ijmecsci.2019.05.041.

[15] H. Mehrabi and I. Aminzahed, "Design and testing of a microgripper with SMA actuator for manipulation of micro components," *Microsyst Technol*, vol. 26, no. 2, pp. 531–536, Feb. 2020, doi: 10.1007/s00542-019-04523-y.

[16] J.-H. Lee, Y. S. Chung, and H. Rodrigue, "Long Shape Memory Alloy Tendon-based Soft Robotic Actuators and Implementation as a Soft Gripper," *Sci Rep*, vol. 9, no. 1, p. 11251, Dec. 2019, doi: 10.1038/s41598-019-47794-1.

[17] J.-H. Guan, Y.-C. Pei, and J.-T. Wu, "A driving strategy of shape memory alloy wires with electric resistance modeled by logistic function for power consumption reduction," *Mechanical Systems and Signal Processing*, vol. 160, p. 107839, Nov. 2021, doi: 10.1016/j.ymssp.2021.107839.

[18] B. Lynch, X.-X. Jiang, A. Ellery, and F. Nitzsche, "Characterization, modeling, and control of Ni-Ti shape memory alloy based on electrical resistance feedback," *Journal of Intelligent Material Systems and Structures*, vol. 27, no. 18, pp. 2489–2507, Nov. 2016, doi: 10.1177/1045389X16633764.

[19] J. Li and H. Harada, "Phase Resistance Feedback Control and Displacement-Resistance Model for Thick SMA Actuator," *JSDD*, vol. 7, no. 2, pp. 197–209, 2013, doi: 10.1299/jsdd.7.197.

[20] N. Michaelis, F. Welsch, S.-M. Kirsch, S. Seelecke, and A. Schütze, "Resistance monitoring of shape memory material stabilization during elastocaloric training," *Smart Mater. Struct.*, vol. 28, no. 10, p. 105046, Oct. 2019, doi: 10.1088/1361-665X/ab3d62.

[21] J. Selvarani Ruth D. and K. Dhanalakshmi, "Shape Memory Alloy Wire for Force Sensing," *IEEE Sensors J.*, vol. 17, no. 4, pp. 967–975, Feb. 2017, doi: 10.1109/JSEN.2016.2642299.

[22] H. Gurung and A. Banerjee, "Self-sensing Shape Memory Alloy wire actuator based on Unscented Kalman Filter," *Sensors and Actuators A: Physical*, vol. 251, pp. 258–265, Nov. 2016, doi: 10.1016/j.sna.2016.09.037.

[23] J. Li and H. Harada, "Phase Resistance Feedback Control and Displacement-Resistance Model for Thick SMA Actuator," *JSDD*, vol. 7, no. 2, pp. 197–209, 2013, doi: 10.1299/jsdd.7.197.

[24] K. C. S. and D. K., "Demonstration of self-sensing in Shape Memory Alloy actuated gripper," in *2013 IEEE International Symposium on Intelligent Control (ISIC)*, Hyderabad, India, Aug. 2013, pp. 218–222. doi: 10.1109/ISIC.2013.6658620.

[25] C.-C. Lan, C.-M. Lin, and C.-H. Fan, "A Self-Sensing Microgripper Module With Wide Handling Ranges," *IEEE/ASME Trans. Mechatron.*,

vol. 16, no. 1, pp. 141–150, Feb. 2011, doi: 10.1109/TMECH.2009.2037495.

[26] F. Simone, G. Rizzello, and S. Seelecke, "Metal muscles and nerves—a self-sensing SMA-actuated hand concept," *Smart Mater. Struct.*, vol. 26, no. 9, p. 095007, Sep. 2017, doi: 10.1088/1361-665X/aa7ad5.

[27] A. Ktena, D. I. Fotiadis, P. D. Spanos, A. Berger, and C. V. Massalas, "Identification of 1D and 2D Preisach models for ferromagnets and shape memory alloys," *International Journal of Engineering Science*, vol. 40, no. 20, pp. 2235–2247, Dec. 2002, doi: 10.1016/S0020-7225(02)00116-7.

[28] M. R. Zakerzadeh and H. Sayyaadi, "Precise position control of shape memory alloy actuator using inverse hysteresis model and model reference adaptive control system," *Mechatronics*, vol. 23, no. 8, pp. 1150–1162, Dec. 2013, doi: 10.1016/j.mechatronics.2013.10.001.

[29] F. Pozo, L. Acho, A. Rodríguez, and G. Pujol, "Nonlinear modeling of hysteretic systems with double hysteretic loops using position and acceleration information," *Nonlinear Dyn*, vol. 57, no. 1–2, pp. 1–12, Jul. 2009, doi: 10.1007/s11071-008-9414-7.

[30] M. Achenbach and I. Müller, "Simulation of material behavior of alloys with shape memory," *Archives of Mechanics*, vol. 37, no. 6, pp. 573–585, 1985.

[31] S. Seelecke and I. Mu¨ller, "Shape memory alloy actuators in smart structures: Modeling and simulation," *Applied Mechanics Reviews*, vol. 57, no. 1, pp. 23–46, Jan. 2004, doi: 10.1115/1.1584064.

[32] B. Malinga and G. D. Buckner, "$\mathscr{L}_1$ adaptive control of a shape memory alloy actuated flexible beam," *Systems Science & Control Engineering*, vol. 3, no. 1, pp. 460–471, Jan. 2015, doi: 10.1080/21642583.2015.1082515.

[33] G. Rizzello, D. Naso, and S. Seelecke, "Hysteresis modeling in thermal shape memory alloy wire actuators: an irreversible port-Hamiltonian approach," 2019.

[34] Q. Ge, H. Qiao, C. Li, Q. Yang, and H. Jiang, "Real-Time Charging Risk Assessment for Electric Vehicles Based on Improved Broad BP-AHP," *IEEE Trans. Ind. Electron.*, vol. 69, no. 9, pp. 9472–9482, Sep. 2022, doi: 10.1109/TIE.2021.3111591.

[35] J. Wu, J. She, Y. Wang, and C.-Y. Su, "Position and Posture Control of Planar Four-Link Underactuated Manipulator Based on Neural Network Model," *IEEE Trans. Ind. Electron.*, vol. 67, no. 6, pp. 4721–4728, Jun. 2020, doi: 10.1109/TIE.2019.2926050.

[36] S. Hochreiter and J. Schmidhuber, "Long short-term memory," *Neural computation*, vol. 9, no. 8, pp. 1735–1780, 1997.

[37] S.-H. Lee and S.-W. Kim, "Improved position control of shape memory alloy actuator using the self-sensing model," *Sensors and Actuators A: Physical*, vol. 297, p. 111529, Oct. 2019, doi: 10.1016/j.sna.2019.111529.

[38] J.-H. Guan, Y.-C. Pei, J.-T. Wu, B.-H. Wang, W.-C. Sui, and S.-R. Li, "A self-sensing and robust resistance phase transition detection method for the displacement estimation of shape memory alloy wires," *Mechanical Systems and Signal Processing*, vol. 170, p. 108862, May 2022, doi: 10.1016/j.ymssp.2022.108862.

[39] J. Khalil-Allafi, A. Dlouhy, and G. Eggeler, "Ni4Ti3-precipitation during aging of NiTi shape memory alloys and its influence on martensitic phase transformations," *Acta Materialia*, vol. 50, no. 17, pp. 4255–4274, Oct. 2002, doi: 10.1016/S1359-6454(02)00257-4.

[40] M. Khosravi, V. N. Behrunani, P. Myszkorowski, R. S. Smith, A. Rupenyan, and J. Lygeros, "Performance-Driven Cascade Controller Tuning With Bayesian Optimization," *IEEE Trans. Ind. Electron.*, vol. 69, no. 1, pp. 1032–1042, Jan. 2022, doi: 10.1109/TIE.2021.3050356.

[41] Y. Wang *et al.*, "Prediction of tubular solar still performance by machine learning integrated with Bayesian optimization algorithm," *Applied Thermal Engineering*, vol. 184, p. 116233, Feb. 2021, doi: 10.1016/j.applthermaleng.2020.116233.

[42] H. Gao *et al.*, "Revolutionizing Membrane Design Using Machine Learning-Bayesian Optimization," *Environ. Sci. Technol.*, vol. 56, no. 4, pp. 2572–2581, Feb. 2022, doi: 10.1021/acs.est.1c04373.

[43] N. Sultana, S. M. Z. Hossain, M. Abusaad, N. Alanbar, Y. Senan, and S. A. Razzak, "Prediction of biodiesel production from microalgal oil using Bayesian optimization algorithm-based machine learning approaches," *Fuel*, vol. 309, p. 122184, Feb. 2022, doi: 10.1016/j.fuel.2021.122184.

[44] I. Ruvinov, N. Zamani, N. Y. Zhou, and M. I. Khan, "Novel laser processed shape memory alloy actuator design with an embedded strain gauge sensor using dual resistance measurements. Part II: Recurrent neural network-based position and force estimation," *Sensors and Actuators A: Physical*, vol. 313, p. 112188, Oct. 2020, doi: 10.1016/j.sna.2020.112188.

[45] G. E. Hinton, N. Srivastava, A. Krizhevsky, I. Sutskever, and R. R. Salakhutdinov, "Improving neural networks by preventing co-adaptation of feature detectors," *arXiv preprint arXiv:1207.0580*, 2012.

Biographical notes

Yong-Chen Pei was born in China in 1980. He received the B.E. degree in mechanical engineering and automation, M.E. and Ph.D. degrees in mechanical design and theory from the Jilin University, Changchun, China in 2003, 2005, and 2008, respectively. From 2013 to 2014, he was a visiting scholar at Engineering Dynamics Research Center in Liverpool University, UK. He is currently a Professor with the School of Mechanical and Aerospace Engineering, Jilin University. His current research interests include engineering calculation and analysis methods, application of smart materials, and intelligent measurement technology.

Bao-Hua Wang was born in Jilin Province, China, in 1997. He received his B.E. degree in mechanical design manufacture and automation from Yanbian University, China, in 2019. His research interests include applications of shape memory alloys.

Ji-Tuo Wu was born in China in 1996. He received the B.E. degree in mechanical engineering from the Jilin University, Changchun, China. His research interests include the application of smart materials.

Chenyang Wang received his BEng degree in Computer Science and Technology from Shanghai Jiao Tong University (SJTU), China, in 2019. He is currently a DPhil candidate in the Department of Engineering Science, University of Oxford, UK. His research interest is machine learning in healthcare.

Jing-Han Guan was born in Liaoning Province, China, in 1997. He received his B.E. degree and M.E. degree from the School of Mechanical and Aerospace Engineering at the Jilin University, China, in 2018 and 2021, respectively. His research interests include actuators based on smart materials.

Huiqi Lu obtained her B.Eng (2004) in Computer Science and Technology in Jilin University, China, and her DPhil (2008) in Industrial Informatics and Signal Processing, University of Sussex. She is a Daphne Jackson and Royal Academy of Engineering Research Fellow at Institute of Biomedical Engineering, Department of Engineering Science, University of Oxford. Her research focuses on AI and mathematical modelling. She is also a Fellow of Higher Education Academy, a Fulford Junior Research Fellow and Governing Body Member of Somerville College, and an Innovation and Enterprise Fellow of University of Oxford. Huiqi serves as a committee member of several international conferences, including IEEE EMBC, NeurIPs, ICLR, and PHM.